Electrostatic charging artefacts in Lorentz electron tomography of MFM tip stray fields

J. Scott, S. McVitie, R. P. Ferrier and A. Gallagher

Department of Physics and Astronomy, University of Glasgow, Glasgow G12 8QQ, UK

Short title: Artefacts in Lorentz tomography of MFM tips

Abstract

Using the technique of differential phase contrast (DPC) Lorentz electron microscopy, the magnetic stray field distribution from magnetic force microscopy tips can be calculated in a plane in front of the tip using tomographic reconstruction techniques. Electrostatic charging of the tip during DPC imaging can significantly distort these field reconstructions. Using a simple point charge model, this paper illustrates the effect of electrostatic charging of the sample on the accuracy of tomographic field reconstructions. A procedure for separating electrostatic and magnetic effects is described, and is demonstrated using experimental tomographic data obtained from a modified MFM tip.

1. Introduction

Magnetic force microscopy (MFM) has proven to be a valuable addition to the range of magnetic microscopy techniques [1,2]. It depends on the principle of scanning a magnetic tip positioned at the free end of a cantilever over the surface of a magnetic sample. Interactions between the tip and the stray fields from the sample are sensed by measuring the deflection or resonant properties of the cantilever. MFM can be performed in air or vacuum, usually with little or no sample preparation required. Quantification of the data thus obtained relies on detailed knowledge of the tip magnetisation, which is normally difficult to obtain using conventional magnetic imaging techniques, as in most cases MFM probes are micron-scale three-dimensional magnetic structures. However, according to reciprocity theory, the MFM signal can also be considered as a convolution of the tip stray field with the sample magnetisation [3]. This approach leads to the conclusion that MFM can be viewed as a form of charge microscopy [4] and hence, if the tip stray field is known, then the magnetic charge distribution of the sample can in principle be determined [5]. Note that quantification of MFM data requires that no tip – sample magnetisation perturbations occur.

The integrated tip stray field can be imaged using the technique of differential phase contrast (DPC) microscopy [6]. This is a variant of Lorentz microscopy, and is implemented in a scanning transmission electron microscope (STEM). Although this is a powerful imaging technique, normally the information obtained only consists of the projection of the stray field. To reconstruct the three-dimensional stray field distribution a tomographic algorithm is used, as demonstrated by Ferrier *et al* [7].

The DPC signal depends on the interaction of an electron beam with the sample magnetic and electrostatic fields. In any individual DPC image it is often impossible to separate the magnetic and electrostatic effects, making interpretation of these images difficult. In this paper these problems are illustrated by numerical modelling. The DPC images obtained from a model MFM tip combined with an electrostatic charge are calculated. The field reconstructions obtained from these model data sets are also calculated and the distortion due to the presence of charging is shown. Using the principle of time reversal on Lorentz microscopy [8,9], a procedure to separate the electrostatic and magnetic contributions in DPC microscopy is outlined. The method is used to determine the electrostatic and magnetic field distributions from a real MFM tip.

2. Experimental details

DPC imaging is performed in a Philips CM20 transmission electron microscope (TEM) equipped with a field emission gun. This microscope can be operated as a scanning TEM (STEM) and has been optimised for imaging magnetic materials [6]. DPC images are acquired by scanning a focussed electron beam in a raster pattern across the sample, as illustrated in figure 1. The presence of magnetic or electrostatic fields deflects the beam by an angle β, according to the equation

$$\beta_{x,y} = \frac{e\lambda}{h}\int_{-\infty}^{\infty} B_{y,x}\,dz + \frac{1}{2V_{accel}}\int_{-\infty}^{\infty} E_{x,y}\,dz \qquad (1)$$

where λ is the wavelength of the electron beam, h is Plank's constant and e is the electronic charge; B is the magnetic induction, E is the electric field and V_{accel} is the beam accelerating voltage. The beam falls onto a quadrant detector situated in the far field and taking difference signals from opposite segments of this detector allows the orthogonal deflection components β_x and β_y to be measured. These signals are digitised and stored for later analysis. The result is a map of the magnetic and electrostatic fields perpendicular to the electron beam direction, integrated along the beam path. The sum of all four quadrant signals simply gives the standard bright field signal, which is useful for alignment purposes and is normally recorded along with the difference signals.

It should be noted that the integration path in equation (1) is an approximation, as the integration should strictly follow the path of the beam. However, for thin magnetic samples the beam will remain approximately parallel to the z axis in the sample region, and outside the sample region the field is assumed to be zero. As an example a uniformly magnetised film of 50 nm

thickness and saturation induction of 1 T will deflect a beam of 200 keV electrons passing through this film by an angle of only 30 μrad. Hence the beam path in the region of the sample is to a close approximation parallel to the optic (*z*) axis of the STEM.

Although DPC images contain useful data, we require the three-dimensional field distribution, rather than the integrated field. To obtain this a tomographic method is used [7]. The sample is rotated around the *y* axis and DPC images are taken at regular angular intervals, usually every 10^0 over a range of 180^0. In these studies the image sampling resolution (pixel spacing) is normally 25-30 nm, and the image size is 256x32 pixels (i.e. a scan width of ~7 μm). The resulting images are aligned using the point of the tip apex as a reference, which can be located using the sum (bright field) images. Linescans are extracted from the corresponding difference images at a distance of ~50 nm from the tip apex. This data is then processed using a tomographic algorithm derived using the relationship between the Radon and Fourier transforms [10,11] (referred to as the RTM alogrithm in ref. 7). The input data are convolved with a kernel that is calculated depending on the experimental conditions and the type of output required. Back projection of the convolved data then yields the field distribution. All three orthogonal field components can be reconstructed using only one component of the deflection data; thus using both deflection components yields two independent field reconstructions.

To help in our understanding of MFM tip behaviour, and to test the accuracy of the reconstruction technique, simple models of the tip magnetisation were constructed by Gallacher [12]. These models comprise uniformly magnetised thin triangular slabs of magnetic material. As can be seen in figure 2(a) these slabs are assembled to form a square based pyramid with dimensions similar to NANOSENSORS™ etched silicon tips (MESP type). The magnetisation of each slab directed towards the tip apex, giving rise to magnetic charges along the edges of the slabs. The model stray field can be then calculated from the resulting charge distribution. Integration of the field along the *z* axis, as shown in figure 2(b) produces the simulated DPC data. Rotating the model tip about the *y* axis and performing the integration every few degrees produces a full tomographic dataset. This data can then be processed by the tomographic alogrithm to yield the field reconstructions. The accuracy of these reconstructions is determined by comparison with the original calculated model field distribution. An important result was obtained by Gallacher using these models; the most accurate tomographic reconstructions are generated from the "opposite" integrated field components. That is to say that the most accurate reconstructions of the *y* component of the field distribution are calculated using the *y* component deflection data (corresponding to the projection of the *x* and *z* field components), and vice-versa. This result has been proven repeatedly by numerical simulation, although there is currently no analytical explanation.

3. Simulation of charging in Lorentz tomography

As with other methods of electron microscopy, electrostatic charging of samples can cause problems in Lorentz microscopy. The effect of electrostatic charge on the electron beam is described in equation (1). Charging can occur if the coating on the MFM tip is poorly conductive, however most MFM tips are coated with some form of reasonably conductive metallic alloy. A more common cause of charging arises from contamination of the sample. If a tip has previously been used in the MFM, it is quite common to observe small particles (dust, for example) attached near to the end of the tip. Contamination can also occur if the beam of the electron microscope is scanned over a small area of the tip for long periods, causing electron beam induced material deposition from residual gases in the microscope vacuum system. However, the vacuum in the CM20 is normally good enough that with care, beam-induced contamination can be minimised. The presence of moderate or heavy contamination is usually obvious when inspecting the bright field images of the tip.

To simulate the effect of charging on the tomographic reconstruction process, an electrostatic charge was added to a model MFM tip of the type described previously. This was achieved by calculating the analytical DPC response from an electrostatic monopole point charge and using the resulting formulae to calculate DPC linescan traces due to the charge. The magnetic and electrostatic data were then combined to form the complete tomographic dataset. The charge was located on the rotation axis, at a distance of 400 nm from the reconstruction plane. (The MFM tip apex was located 60 nm from the

reconstruction plane). This was done for charges of varying magnitude (-3.8×10^{-11}, -7.8×10^{-11} and -15.5×10^{-11} Coulombs). These model parameters were chosen so that the resulting DPC data was of similar character to experimental data taken in previous studies where charging was obviously present, due to tip contamination by dust particles. Selected linescans from the resulting datasets are displayed in figure 3 for (a) MFM tip only and (b) MFM tip and charge of -7.8×10^{-11} C.

The DPC data from these models were input to the tomographic alogrithm, treating the data as though it were purely magnetic in origin, and the magnetic fields from the models were reconstructed. The reconstructed field distributions are shown in figure 4 for the (a) uncharged and (b) charge equal to -7.8×10^{-11} C models. The reconstruction from the purely magnetic data is very close to the actual model field (Gallacher showed that the reconstruction error of the peak field magnitude is less than 5% using this reconstruction technique). By contrast, it is obvious that there are significant artefacts in the reconstruction of the model with charge added.

In the MFM the force or force gradient acting along the tip axis is sensed. This signal will depend on the interaction of the magnetic charge distribution in the sample with the component of the tip stray field parallel to the tip axis. This means that the *y* field component of the tip stray field is the most relevant to MFM, and hence further analysis was concentrated on the *y* field components of the reconstructions. Linescans of the y field component through the reconstruction centre along the *z* axis are shown in figure 5 for varying charge. These scans clearly illustrate the increasing distortion of the reconstruction with charge magnitude. It can be seen that although the peak position and height is largely unaffected, the shape of the peak is distorted markedly. The equivalent linescans along the *x* axis (not shown) were unaffected by the presence of electrostatic charge.

It is obviously desirable to be able to separate the magnetic and electrostatic effects. Other authors [8,9] have discussed several solutions to this problem. The method used in both references is to utilise the effect of time reversal on the phase contrast of the specimen. The simplest way to achieve this is to take two images of the specimen, turning the specimen upside down for the second image. Using these two images the magnetic and electrostatic contributions to the phase contrast image can be separated. This can be explained as follows. Consider a point of a thin sample at coordinates (x_0, y_0). At this point the deflection of the electron beam in the *x* direction (β_x) is proportional to the integrated *x* electrostatic field component (E_x) and the integrated *y* magnetic field component (B_y). If the sample is then rotated 180^0 around the *y* axis, the point of the sample under consideration will now be located at ($-x_0$, y_0). At this point E_x will reverse in direction, while B_y will still point in the same direction as before. Hence, we can say that the sign of the electrostatic contribution to β_x changes with the sample rotation, while the sign of the magnetic contribution stays the same. Adding and subtracting the β_x signals taken at 0^0 and 180^0 then yields $2B_y$ and $2E_x$ respectively at the point of the sample under consideration. Similarly, the β_y signals yield $2E_y$ and $2B_x$.

It should be noted that this procedure is only valid if the electrostatic and magnetic field distributions are the same for both sample positions. As the DPC imaging is performed in magnetic field-free conditions, it is certainly the case that the magnetisation of the tip will be undisturbed by sample rotation. The amount of charging in each image should also be similar given that the imaging conditions (beam current and size, scan speed and size) are the same for both images, and the tip apex is to a good approximation cylindrically symmetric. The charging characteristics may be different if contamination of the tip occurs between acquisition of the images, but this problem can usually be avoided if care is taken to minimise the exposure of the tip to the electron beam.

There are other methods to separate the magnetic and electric components in DPC imaging. In particular, the ratio of magnetic to electric contributions in the DPC signal changes with the electron beam accelerating voltage, and so in principle obtaining two DPC images at different accelerating voltages allows separation. However, as the imaging conditions in the microscope also change with the accelerating voltage, this method is impractical to implement and is not considered here.

4. Experimental case study

To test the effectiveness of the separation procedure outlined above an extended tomographic dataset was taken of a MFM tip. The tip used was a NANOSENSORS™ MFM tip modified by ion beam milling (figure 6). This tip possesses a spike several microns long, and was coated by evaporation on the front side of the spike with 25 nm of Co. It was felt that this thickness of Co, along with the spike geometry would result in a smaller stray field than standard Nanosensors MFM tips, hence allowing easier observation of any charging effects. The tip was magnetised along the spike axis by a 1 T field before being placed in the STEM. DPC images were taken every 10^0 as the tip was rotated from 0^0 to 350^0.

Sample linescans are shown in figure 7(a), taken at the 90^0 and 270^0 rotation positions. It can be seen that the form of these linescans is not what would be expected from an axially magnetised spike tip. Indeed, at first glance the linescans have the form that would be expected from a tip magnetised along the cantilever axis, i.e. across the tip. The data was analysed using the procedure outlined earlier. Each linescan in the first 180^0 of data was subtracted from its counterpart taken from the diametrically opposite position. Results from this processing stage are shown in figure 7(b).

There are a number of points of interest in this data. Examining the data in figure 7(b), it is apparent that the magnitude of the DPC signal due to electrostatic effects is at least twice as large as the magnetic signal. It is also notable that the electrostatic peak is centred almost exactly at the origin and is symmetrical about the origin, implying that the electrostatic charge is distributed symmetrically over the tip. The width of the peak is similar to the DPC signal calculated from the point charge model used earlier, implying that the charge is concentrated at or near the tip apex. The magnetic signal is also well defined, and is consistent with what would be expected from a spike tip magnetised along its long axis. These results indicate that there can be a significant amount of electrostatic charging present in tomographic studies, even if the MFM tip is considered to be reasonably conductive (as in this case).

It is also apparent that both the unprocessed and processed linescan sets have some degree of d.c. shift associated with them, as reported previously by Ferrier *et al* [7]. The cause of these d.c. shifts (for the magnetic case) has been investigated by Gallacher, and was attributed to the fields from the magnetic material coating the cantilever and supporting substrate of the tip. The fields produced by these elements are usually of low magnitude at the reconstruction plane. However, the spatial extent of these fields is much greater than that of the tip (in the case of the substrate coating, the field produced can extend over a few mm). As DPC imaging integrates the field over the whole beam path, the cantilever and substrate fields can produce a large, albeit slowly varying contribution to the DPC data. However, as noted earlier, reconstructing the y field component from the projections of the *x* field component results in high accuracy. Gallacher showed that this is true even with large level shifts in the DPC data, and so we can be confident that the reconstructions presented here are true descriptions of the field distribution, assuming that the input data are purely magnetic in origin. The reconstructions of the tip stray field are shown in figure 8 for (a) the original unprocessed data and (b) the separated magnetic data. Linescans of the *y* field components of these reconstructions along the *z* axis are shown in figure 9.

As expected, the reconstruction from the unprocessed data exhibits a smearing effect in the *z* direction, consistent with the charged simulations examined in the previous section. The form of the field in the centre of the reconstruction could potentially be due to a magnetic dipole at a short distance from the reconstruction plane (corresponding to the tip being magnetised perpendicular to the spike direction). However, the long tails extending from the centre of the reconstruction are entirely inconsistent with the geometry of the tip. The linescans along the *z* axes of the reconstructions show this point clearly, and illustrate the severe distortion induced by the electrostatic effects. The reconstruction from the processed data shows a field distribution much closer to that expected from an axially magnetised spike tip, with a peak field of 8.1 mT and a full width at half maximum (FWHM) of 290 nm (for the *y* field component).

The separation procedure used here yields as a by-product the DPC data set due to the electrostatic field only, also over a rotation range of 180^0. It is possible to reconstruct electrostatic fields using the same tomographic alogrithm as used for magnetic data, as the mathematical properties of magnetic and electric fields are the same in vacuum. The only differences are that the units involved are different and the input deflection data components must be swapped round (compared with the magnetic configuration of the alogrithm). The reconstruction of the electric field from the tip is shown in figure 10. The electrostatic field

distribution is centred on the rotation axis, and more detailed analysis shows that the field is roughly circularly symmetric. The peak height is approximately –4.5 Vnm^{-1} and the FWHM is 400 nm. The width of the peak and the absence of background field suggests that the electrostatic charge on the MFM tip is indeed concentrated near the tip apex, as might be expected. To test this hypothesis a point charge model was fitted to the electrostatic data, the two fitting parameters being the distance of the charge to the reconstruction plane and the magnitude of the charge. A very close fit was obtained for a point charge of $5x10^{-14}$ C at a distance of 320 nm, which compares favourably with the parameters used for the simulations in the previous section. This result implies that the charge density is highest within a few hundred nm of the tip apex, possibly due to contamination around the tip apex.

The electrostatic effects in this study are slightly larger than anticipated by the simulations shown earlier. Other tomographic studies of MFM tips performed previously have not exhibited such extreme effects [7,13]. However, careful examination of the data for the 50 nm METGLAS tip in ref. 13 (for example) does reveal evidence of a small amount of charging, centred on the rotation axis. Examination of the deflection data used in that study indicates that the magnitude of the Lorentz deflection signal due to electrostatic charge was slightly less than half than that of the magnetic signal. Thus the effect is not readily apparent in the linescans of the reconstruction shown in that work, mainly because the amount of charging was not excessive and the linescans are taken along the *x* axes of the reconstructions. As illustrated earlier, if the electrostatic charge of the tip is centered on the rotation axis, the linescan along the *x* axis of the reconstruction is unaffected. Furthermore, the magnetic peak was much sharper than the electrostatic, so the electrostatic signal acted more as a spurious background signal. Thus the linescans shown in ref. 13 still represent the character of the tips in that study, although the values of the field peaks may not be as accurate as first thought.

The degree of charging present in this study is therefore somewhat atypical, and can be considered as a more extreme case. Nevertheless, this analysis shows that the ability to separate the magnetic and electrostatic components in tomography is very useful, and should probably be done as routine, especially when imaging tips with small magnetic moments and stray fields. Charging problems will not be as apparent when imaging high magnetic moment tips, simply because the large magnetic fields will dominate the DPC data in these cases (as long as the amount of charging is comparable to this study). For example, the field reconstruction of the CoCr coated MFM tip in ref. 7 exhibits no obvious charging artefacts.

The main disadvantage of the seperation method used here is the requirement that a full 360^0 tomographic dataset be taken, as opposed to the 180^0 datasets normally used. This requires several hours of data collection and necessitates four sample position changes (see ref. 7 for details). However, the symmetry and central location of the charge distribution suggests that it may only be necessary to find the electrostatic components of the DPC signal at one or two angular positions. Assuming that the charge distribution is indeed symmetric about the rotation axis, the electrostatic signal thus found can then be subtracted from the data over the entire range of rotation, leaving the magnetic components only. This assumption allows the analysis to be carried out on previous studies, as in most cases data for tomography was collected over a range of 190^0 (the total rotation range accessible with one change of the sample stub position). Initial analysis of tomographic data acquired in earlier experiments indicates that in most cases there is some degree of charging (even when the tip has been gold coated to try and prevent this problem), and the electrostatic contribution is usually symmetric about the rotation axis. This will therefore allow us to improve the accuracy of studies already performed, confirming that this analysis should be done as routine, particularly for tips with low magnetic moments.

5. Conclusions

We have demonstrated the effects of electrostatic charging on Lorentz tomographic reconstructions of stray fields using a simple monopole point charge model and a simulated MFM tip. Comparison to experimental data has shown that a point charge model can be sufficient to describe electrostatic charging of the tip. It has been shown that given sufficient data, it is possible to

separate these magnetic and electrostatic effects. These findings will therefore improve the accuracy of Lorentz tomographic studies of MFM tips.

Acknowledgements

This work was supported by the United Kingdom EPSRC under grant number GR/L42896. The authors would like to thank Liesl Folks (IBM Almaden Research Center) who kindly supplied the modified MFM tip.

References

[1] Y. Martin and H. K. Wickramasinghe, "Magnetic Imaging by Force Microscopy with 1000-A Resolution", *Appl. Phys. Lett.* **50**, 1455 (1987)

[2] D. Rugar, H. J. Mamin, P. Guethner, S. E. Lambert, J. E. Stern, I. McFadyen and T. Yogi, "Magnetic force microscopy: General principles and application to longitudinal recording media", *J. Appl. Phys.*, **68**, 1169 (1990)

[3] C. D. Wright and E. W. Hill, "Reciprocity in magnetic force microscopy," *Appl. Phys. Lett.*, vol 67, pp. 433-435, 1995

[4] A. Hubert, W. Rave and S. L. Tomlinson, "Imaging Magnetic Charges with Magnetic Force Microscopy", *Physica Status Solidi B*, **204**, No.2, 817 (1997)

[5] Chang T, Mark L, Zhu J and Judy J H (1992), "Deconvolution of Magnetic Force Images by Fourier Analysis", *IEEE Trans. Magn*., **28**, 3138

[6] J. N. Chapman, "The Investigation of Magnetic Domain-Structures in Thin Foils by Electron-Microscopy", *J. Phys. D: Appl. Phys.*, **17**, 623 (1984)

[7] R. P. Ferrier, S. McVitie, A. Gallacher and W. A. P. Nicholson, "Characterisation of MFM tip fields by electron tomography," *IEEE Trans. Magn.*, **33**, 4062 (1997)

[8] A. Tonomura, T. Matsuda, J. Endo, T. Arii and K. Mihama, "Holographic interference electron microscopy for determining specimen magnetic structure and thickness determination", *Phys. Rev. B*, **34**, 3397 (1986)

[9] B. G. Frost and T. L. Jenkins, "On the interpretation of magnetic and electric fields imaged by low-magnification off-axis electron holography", *J. Microsc.*, **187**, 85 (1996)

[10] M. Steck, "Quantitative Bestimmung magnetischer und elektrischer Mikrofelder mit Hilfe der Elektronenstrahl-Tomografie", *Doctoral Thesis*, Duisburg University (1990)

[11] J. B. Elsbrock, W. Schroeder and E. Kubalek, "Evaluation of Three-Dimensional micromagnetic Stray Fields by Means of Electron-Beam Tomography", *IEEE Trans. Magn*., **MAG-21**, 1593 (1985)

[12] A. Gallacher, "Theoretical Characterisation of Magnetic Force Microscope Tip Stray Fields", *Ph.D. Thesis*, Glasgow University (1999)

[13] J. Scott, S. McVitie, R. P. Ferrier, G. P. Heydon, W. M. Rainforth, M. R. J. Gibbs, J. W. Tucker, H. A. Davies and J. E. L. Bishop, "Characterisation of FeBSiC coated MFM tips using Lorentz electron tomography and MFM", *IEEE Trans. Mag*. **35**, 3986 (1999)

Figure captions

Figure 1. Diagram illustrating the principle of DPC imaging in the STEM.

Figure 2. Diagram showing (a) Configuration of model MFM tip used for simulations and (b) Orientation of tip in the STEM for tomography. The tip axis makes an angle of 12.5^0 with the *y* (rotation) axis.

Figure 3. DPC linescans (*y* deflection component) from model MFM tip with (a) no electrostatic charge and (b) with electrostatic point charge of $-7.8\text{x}10^{-11}$ Coulombs. The magnetic model was of a pyramidal tip with uniformly magnetised triangular prism thin films on each face of the tip extending to a distance of *h* from the tip apex. In this case *h* was 15 μm, and the films were 40 nm thick Co, magnetised in the plane of the film and pointing towards the tip apex as shown in figure 2(a). Linescans are shown for tip rotations of 0^0, 45^0, 90^0 and 135^0. Extended charge model.

Figure 4. Magnetic field reconstructions calculated from the data shown in figure 3. Reconstruction (a) is for model with no electrostatic charge, (b) for an electrostatic charge of $-7.8\text{x}10^{-11}$ C. Field components are (from left to right) *x*(⇔), *z*(⇳), *y*(⊙).

Figure 5. Linescans of the reconstructed field for tip models with charges of 0, $-3.8\text{x}10^{-11}$, $-7.8\text{x}10^{-11}$ and $-15.5\text{x}10^{-11}$ C. The linescans are taken along the *z* axis of the *y* field component

Figure 6. Scanning electron microscope image of modified MFM tip, showing the FIB milled spike.

Figure 7. Sample of DPC data taken from modified MFM tip, showing the *y* deflection signal. (a) Original DPC linescans taken at 90^0 and 270^0 rotation. (b) DPC linescans separated into magnetic (B_x) and electrostatic (E_y) components.

Figure 8. Reconstructions of the magnetic stray field from the modified MFM tip using (a) the original unprocessed data and (b) the separated magnetic data. Field components are (from left to right) *x*(⇔), *z*(⇳), *y*(⊙).

Figure 9. Linescans along the z axes of the y field component from figure 8(a) (unprocessed data) and figure 8(b) (processed data).

Figure 10. Reconstruction of electrostatic field from modified MFM tip. Field components are (from left to right) *x*(⇔), *z*(⇳), *y*(⊙).

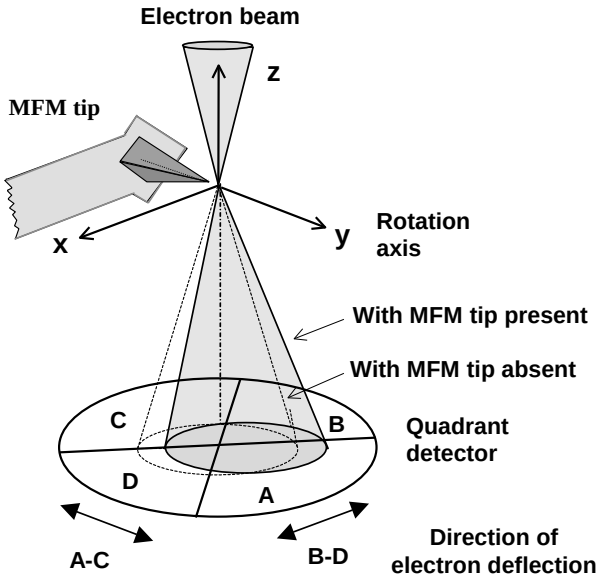
Electron beam
z
MFM tip
x
y
Rotation axis
With MFM tip present
With MFM tip absent
C
B
D
A
Quadrant detector
A-C
B-D
Direction of electron deflection

Figure 1

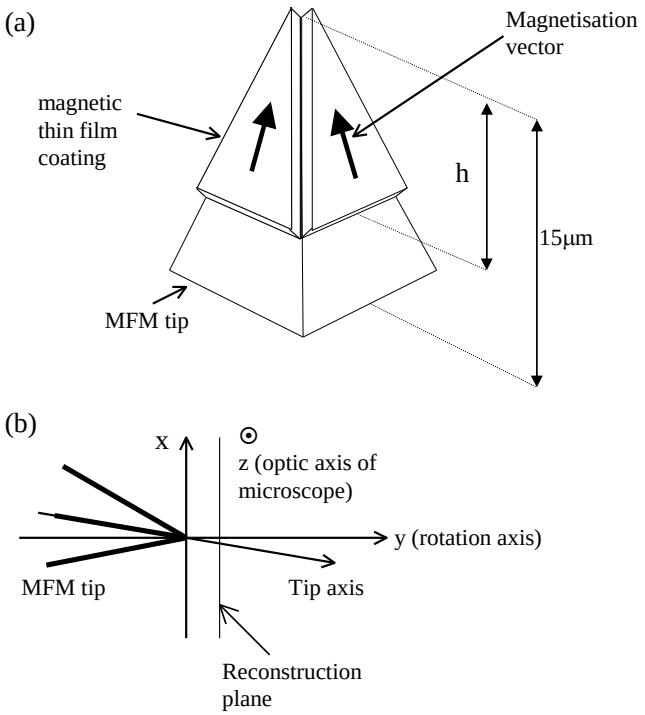
(a)
Magnetisation vector
magnetic thin film coating
h
15μm
MFM tip
(b)
x
z (optic axis of microscope)
y (rotation axis)
MFM tip
Tip axis
Reconstruction plane

Figure 2

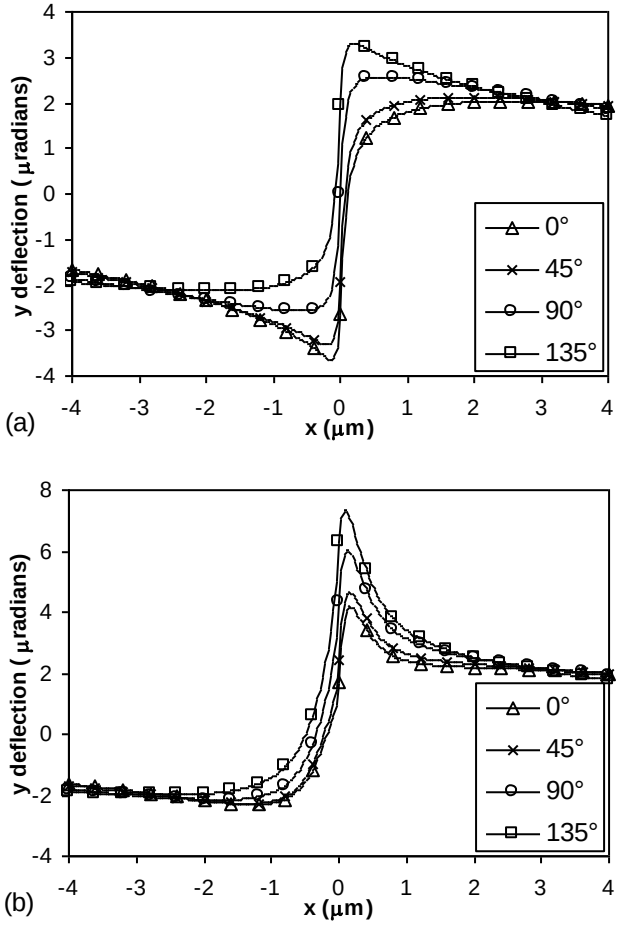
y deflection (μradians)
x (μm)
0°
45°
90°
135°
(a)
y deflection (μradians)
x (μm)
0°
45°
90°
135°
(b)

Figure 3

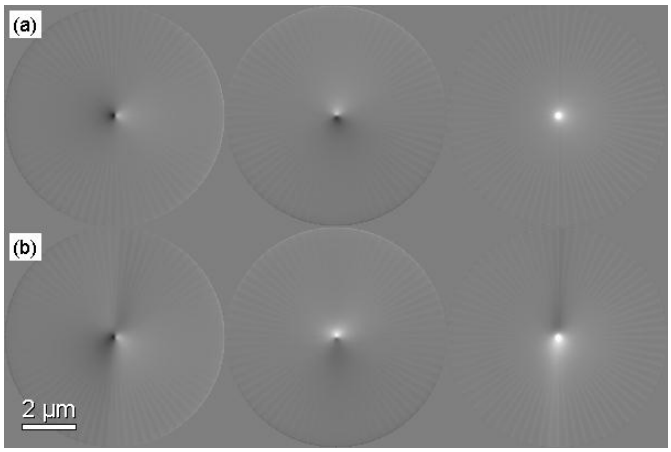

Figure 4

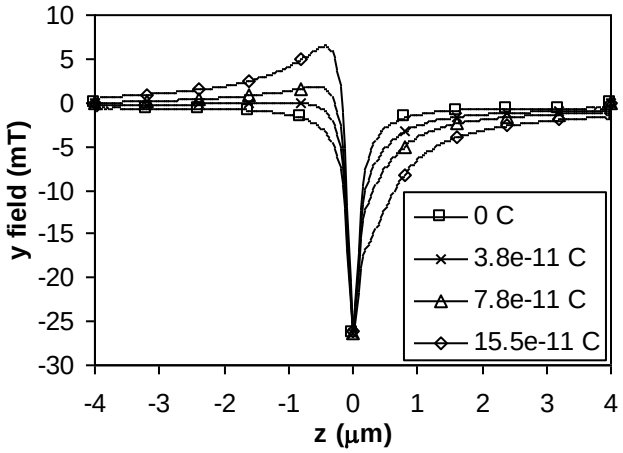
10
5
0
-5
-10
-15
-20
-25
-30
y field (mT)
-4
-3
-2
-1
0
1
2
3
4
z (μm)
0 C
3.8e-11 C
7.8e-11 C
15.5e-11 C

Figure 5

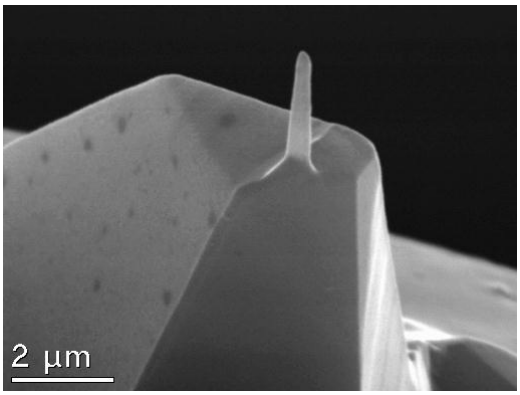

Figure 6

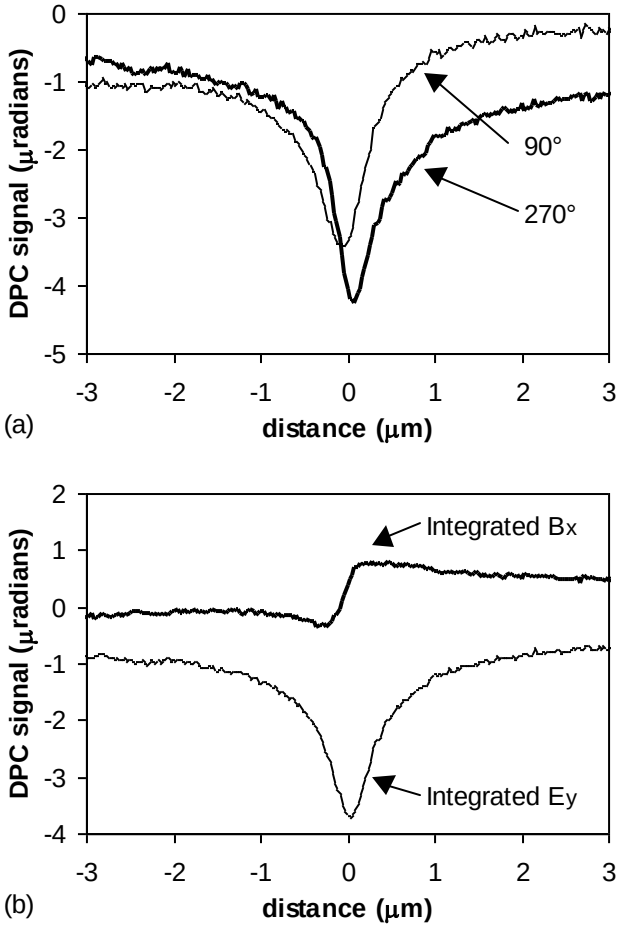
0
-1
-2
-3
-4
-5
DPC signal (μradians)
90°
270°
-3
-2
-1
0
1
2
3
distance (μm)
(a)
2
1
0
-1
-2
-3
-4
DPC signal (μradians)
Integrated Bx
Integrated Ey
-3
-2
-1
0
1
2
3
distance (μm)
(b)

Figure 7

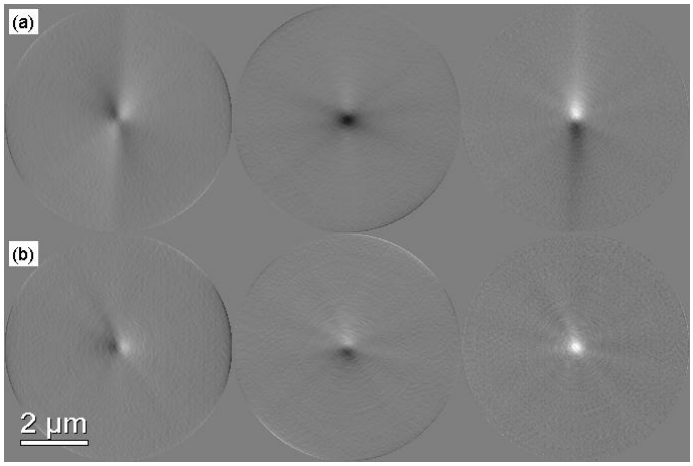

Figure 8

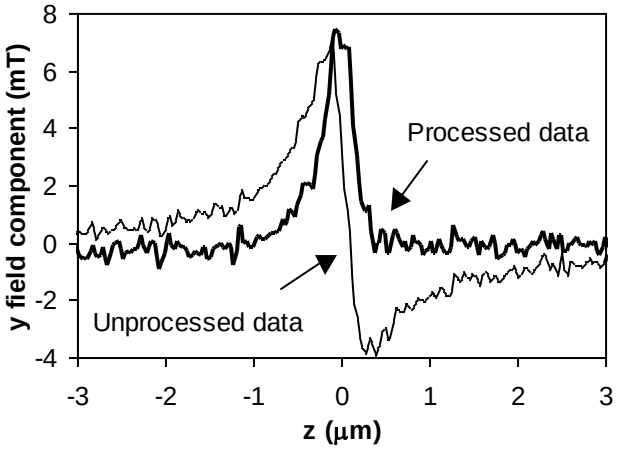
y field component (mT)
8
6
4
2
0
-2
-4
-3
-2
-1
0
1
2
3
z (μm)
Processed data
Unprocessed data

Figure 9

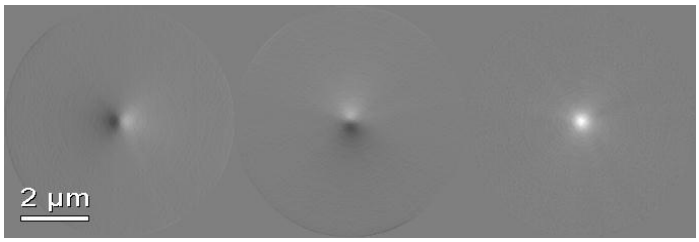

Figure 10